Passive multi-static SAR - experimental results

Nithirochananont, Ussanai; Antoniou, Michail; Cherniakov, Mikhail

DOI:
10.1049/iet-rsn.2018.5226

Document Version
Peer reviewed version

Citation for published version (Harvard):
Nithirochananont, U, Antoniou, M & Cherniakov, M 2019, 'Passive multi-static SAR - experimental results', *IET Radar, Sonar and Navigation*, vol. 13, no. 2, pp. 222-228. https://doi.org/10.1049/iet-rsn.2018.5226

Passive Multistatic SAR - Experimental Results

Ussanai Nithirochananont, Michail Antoniou [*], and Mikhail Cherniakov

[1] Department of Electronic, Electrical and Systems Engineering, University of Birmingham, Edgbaston B15 2TT, Birmingham, United Kingdom
[*]m.antoniou@bham.ac.uk

Abstract: This paper experimentally explores the potential of passive multistatic SAR imaging. An experimental campaign was conducted with navigation satellites (e.g. GPS) as transmitters of opportunity. During the experiment, a single receiver recorded satellite signal reflections off a target area from 4 satellites in its field of view. Based on the total recording time and the number of signals processed, a total of 46 bistatic images were obtained. Subsequently, those bistatic images were non-coherently combined into a single multistatic image. The obtained results show that the multistatic image enhances target area information space and can additionally be used to reveal object geometric features such as edges, shape, and dimensions, which are otherwise difficult to observe in passive SAR with its modest spatial resolution. In addition, information obtained from individual images was combined to understand whether or not different object types can be classified based on variations of their bistatic reflections, with promising first results.

1. Introduction

Passive Synthetic Aperture Radar (SAR) has recently received increased attention. In this configuration, an illuminator of opportunity, typically ground-based or spaceborne, is used as the transmitting source. A receiver tuned to the transmit signal characteristics can then record signal reflections off a target area, and process them to form a SAR image of the scene. The synthetic aperture itself can be formed by the motion of either or both the transmitter and the receiver. A number of experimental radar images have been obtained from a variety of illuminating sources and receiver configurations [1]-[3].

This paper considers passive SAR with Global Navigation Satellite System (GNSS) illuminators (such as GPS or Galileo) and a fixed receiver on the ground. This topical area has been considered for a number of years on the theoretical and experimental levels using a single satellite and a single receiver [4], [5]. The main peculiarity of this system is that since the power flux density of the satellites near the ground is relatively low, its operational range is in the order of a few kilometres. This is achieved with long dwell times on target, which are in the order of several minutes, since the satellites are on Medium Earth Orbit (MEO). Using a single GNSS ranging signal, the maximum signal bandwidth can be approximately 10 MHz, providing a quasi-monostatic range resolution of 15 m, although it has been possible to combine adjacent Galileo bands for an aggregate bandwidth of 50 MHz [6], [7].

At the same time, GNSS have a global and persistent coverage, hence providing the potential for persistent local area monitoring anywhere in the world. In addition, in radar terms GNSS are multistatic systems. This is because at any point on Earth, at any time of day, 6-8 satellites from a single constellation are illuminating the same area from different aspect angles simultaneously, and all these signals can be recorded and processed by a single receiver in a similar fashion to navigation purposes.

Having experimentally confirmed the feasibility of GNSS-based SAR with a single satellite, the natural continuation of this work is to consider its multistatic operation. This entails the acquisition of multiple GNSS-based SAR images (Fig.1), and their combination.

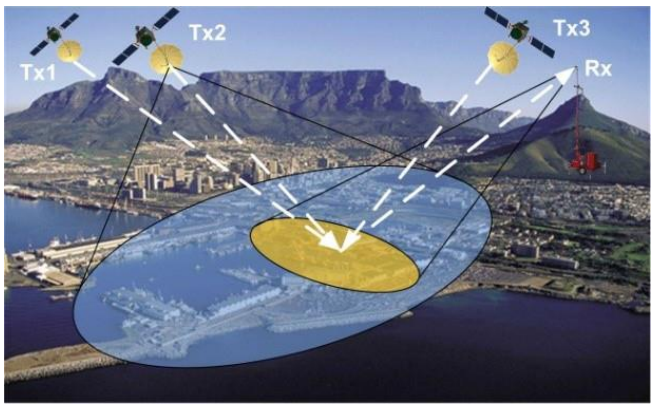

Figure 1: The concept of passive multistatic SAR with GNSS transmissions

Some research in this area has recently been done. In [8], it was shown that combining bistatic SAR images from two satellites under specific acquisition geometries can improve image spatial resolution by a factor of up to 5, but artefacts exists which should be corrected. In [9], great promise was shown by applying image fusion techniques, but with several limiting factors as a first step in this research, such as using a single GNSS system (Beidou), similar satellite orientations in azimuth, and bistatic imagery obtained with temporal separations of up to a month.

The goal of this paper is to experimentally explore multistatic passive SAR, and to understand how it may be able to enhance image information space compared to a bistatic image. This is done by a dedicated experimental campaign, with signals simultaneously acquired from 4 different satellites belonging to two different GNSS constellations (GPS and Galileo) over the span of a few hours, and taking into account the spatial diversity offered by them. As there is little control on the GNSS orbits required for a coherent image combination, a non-coherent scheme is investigated instead as a first step.

It is highlighted that work done here and its findings are not just applicable to GNSS, but to any multistatic SAR, active or passive.

The paper is organised as follows: Section 2 briefly describes image formation in GNSS-based bistatic SAR and the combination of multiple bistatic images can form a multistatictic image. In Section 3, the experimental campaign is presented. Finally, Sections 4 and 5 show and discuss bistatic and multistatic experimental results, respectively.

2. Bistatic Imaging and Non-coherent Image Combination

2.1. Bistatic Image Formation

The process of forming images using a GNSS-based bistatic SAR has already been established. Moreover, the emphasis of the paper is on experimental, rather than theoretical analyses. Therefore, only a brief overview of the characteristics of this system is provided here prior to multistatic imaging. The reader is prompted to [4], [10], [11] for detailed descriptions.

Typically, the SAR receiver comprises two channels (Fig.2). The first one, called the Heterodyne Channel (HC), has a low-gain antenna pointed towards the sky to record the direct signal from the satellite for signal synchronisation purposes. The second channel, called the Radar Channel (RC), has a higher gain antenna pointed towards the target area for imaging. Signal synchronisation is required to maintain the coherence required for image formation, and is implemented in practice by tracking the direct signal of the satellite in a similar, if not identical, fashion to GNSS tracking for navigation. This process can be simplified because unlike other transmitters, such as digital television, GNSS spreading codes are known. At the output of this operation, a locally generated replica of the direct signal, consisting of the GNSS spreading code, and the tracked direct signal parameters, is used for range compression with reflected signal data in the RC. Range-compressed data can then be processed with a back-projection algorithm (requiring knowledge of the transmitter and receiver positions) to form passive SAR imagery.

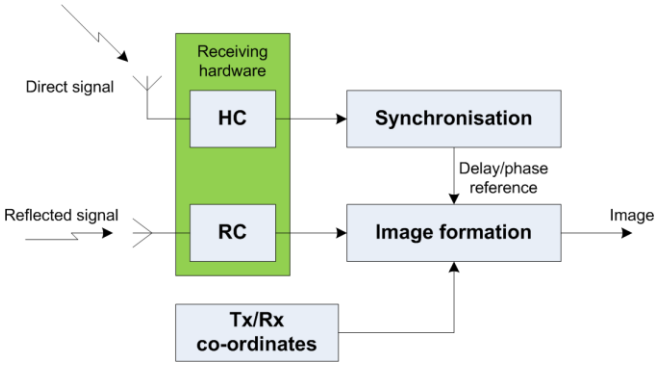

Figure 2: Block diagram of bistatic imaging

2.2. Non-coherent Multistatic Imaging

GNSS employs multiple access schemes (code or frequency division) and pseudo-random spreading codes to separate signals from different satellites. Therefore, despite the receiver collects all signals from all satellites in its field of view simultaneously, those can be separated at the signal processing level. This means that by repeating the process described above for all available satellites, a set of corresponding bistatic images can be formed. Taking into account a bistatic transmitter-receiver pair, the final image can be written as the superposition of the Point Spread Function (PSF) of all scatterers in the scene. Assuming a discrete number of K scatterers for simplicity, this can be written as:

$$I_i = \sum_{k=1}^{K} S_{i,k} = \sum_{k=1}^{K} \xi_{i,k} \chi_i(x - x_k, y - y_k) \qquad (1)$$

where I_i is a bistatic image obtained from i^{th} bistatic image, $S_{i,k}$ is bistatic response, $\xi_{i,k}$ is a complex amplitude of the scatterer reflectivity, and $\chi_i(\cdot)$ is the PSF. The PSF for a bistatic SAR, including GNSS-based SAR, has been theoretically derived [12] and experimentally confirmed [5].

Since our focus is on imagery acquired by multiple transmitters simultaneously illuminating an area, relative satellite and receiver positioning that could enable a coherent combination of images is possible but unlikely. For this reason, a non-coherent combination scheme is considered, implemented simply by adding the complex magnitudes of each bistatic image pixel. It should be mentioned here that each bistatic image is computed in the same ground reference grid, so there is no need for image co-registration prior to this operation. Hence, the multistatic image can be written as:

$$\begin{aligned} I_M &= \frac{1}{N} \sum_{i=1}^{N} |I_i| \\ &= \frac{1}{N} \sum_{i=1}^{N} \sum_{k=1}^{K} |S_{i,k}| \\ &= \frac{1}{N} \sum_{i=1}^{N} \sum_{k=1}^{K} A_{i,k} |\chi_i(x - x_k, y - y_k)| \end{aligned} \qquad (2)$$

where I_M is a multistatic image and $A_{i,k} = |\xi_{i,k}|$ is amplitude of the scatterer reflectivity in the i^{th} image.

3. Experimental Campaign

3.1. Experimental System

An experimental campaign was conducted to experimentally explore additional capability that could be offered with a passive multistatic SAR system compared to a bistatic one. Experiments were done with a single receiver, installed on the roof of 35-metre tall building at the University of Birmingham (Fig. 3). The receiver was the SX-3 by IFEN GmbH, which is a software-defined radio receiver originally designed for navigation purposes but specially modified as a SAR receiver [7]. The receiver records direct and reflected signals through separate channels, and performs signal synchronisation for all satellites in near real-time. Image formation, on the other hand, was done offline.

Figure 3: Experimental system

3.2. Target Area

The target area, a part of the university campus, is shown in Fig. 4. The left part of the area resembles an urban environment, whereas the right part is more indicative of a rural area with trees and sparse buildings. Distinctive features of the area include sports fields, residence towers (~1.2 km range) marked as target (A), tree lines (at 700 to 900 m range) marked as target (B), as well as different complex buildings on the lower-left part of Fig. 4, which are the university's Medical School, Women's Hospital (C), multi-storey car park (E), Medical School and Institute of Biomedical Research (D), Institute of Translational Medicine (F), and Queen Elizabeth Hospital Birmingham Charity (G).

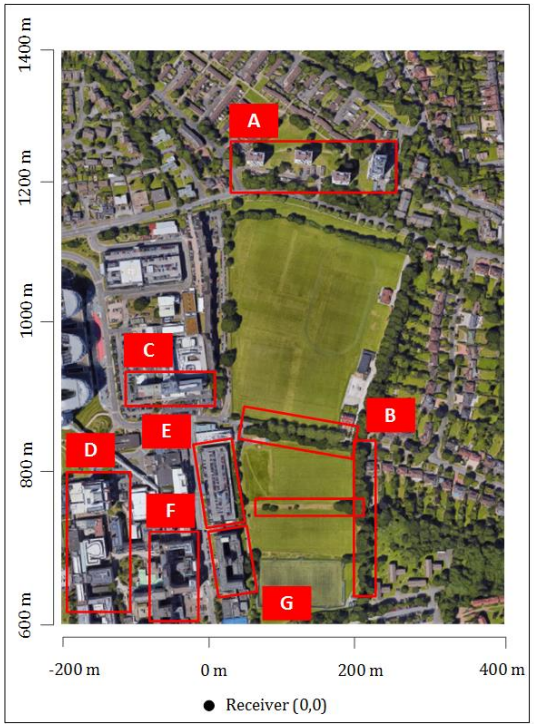

Figure 4: Target area with the location of the receiver

3.3. Data Collection

Satellite signals from two GPS satellites (BIIF-05-30 and BIIF-07-09) and two Galileo satellites (GSAT-0205-E24 and GSAT-0214-E05) were acquired. These signals were recorded in a blocks of 10 mins, which was the coherent dwell time on target. Each data block was followed by a 5-minute gap. A sky map of satellite trajectories during the time of measurement are shown in Fig. 5. The other satellite parameters are listed in Table 1, with notation of satellite azimuth and bistatic angles shown in Fig. 6. Note that bistatic angle is defined as the angle between the transmitter and receiver lines of sight to the centre of the target area, at the midpoint of the transmitter's flight path (i.e. the centre of the synthetic aperture). The table shows that measurements over a variety of relative satellite azimuth and elevation angles were made, with a total azimuth span between 48 and 203 degrees and a total elevation span from 26 to 80 degrees. The bandwidth of all satellite signals is 10.23 MHz, resulting in a quasi-monostatic range resolution of 15 m. The satellites used were chosen because they were in the general area behind the receiver (note however the bistatic angle is outside the quasi-monostatic region), which reduced further degradation in the range resolution due to the bistatic geometry.

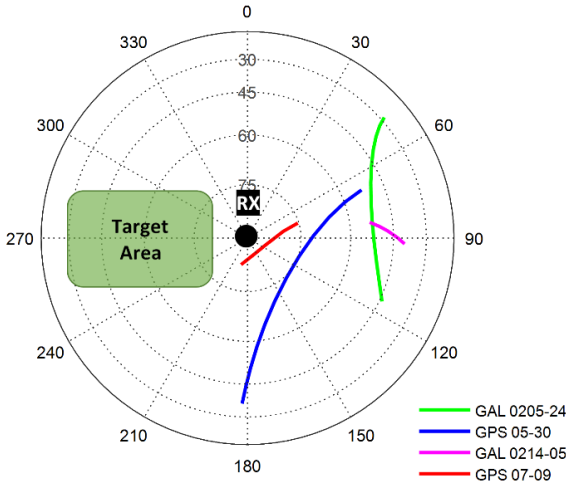

Figure 5: Satellite trajectories during the measurement

4. Bistatic Results

A total of 46 experimental bistatic images were obtained from the system under imaging geometry in Fig. 6. Examples of obtained bistatic images obtained from different satellites with different bistatic and azimuth angles over the total observation period are shown in Figs. 7, superimposed on a Google Earth photograph of the scene to pair radar returns with their corresponding targets. The span in θ quoted in the figures corresponds to the angular interval of observation during data acquisition. All images were normalised to the same value (that of the highest compressed direct signal among those bistatic images) to enable a direct comparison of the relative intensities across the images, and plotted in dB with a dynamic range clipped to 35 dB.

The figures show that bistatic images of the same target area can substantially differ depending on the relative satellite orientation, which is expected since the satellite illumination is at different angles. Scattering properties of an object, especially a building, varied with different imaging geometries despit using same satellite.

Table 1: GNSS signals characteristic and experimental parameters

Parameter	GPS BIIF-05-30	Galileo GSAT-0205-E24		GPS BIIF-07-09	Galileo GSAT-0214-E05
Signal	L5	E5a	E5b	L5	E5a
Modulation	BPSK	AltBOC	AltBOC	BPSK	AltBOC
Carrier Frequency (MHz)	1176.45	1176.45	1207.14	1176.45	1176.45
Ranging Code Bandwidth (MHz)	10.23	10.23	10.23	10.23	10.23
Dwell Time (s)	600	600	600	600	600
Azimuth, [θ] (Degree)	182.19 – 66.67	117.24 – 48.36		203.39 – 71.99	81.51 – 93.33
Elevation (Degree)	34.34 – 51.00	42.55 – 26.37		80.30 – 72.97	55.04 – 38.84
Bistatic Angle, [β] (Degree)	91.51 – 56.49	49.35 – 48.54		91.80 – 75.90	53.74 – 40.47

This is much more prominent in the left part of the image where there are more dense building structures, so apart from bistatic scattering differences there is the additional problem of shadowing. The shadowing also anticipated from buildings beyond area C, where they are lower than those in the lower left part of the image. In addition, as the spatial resolution of the passive SAR is modest, and the system sensitivity is limited due to the low satellite power flux density near the ground, only the strongest returns at a particular scattering angle can be seen, so even returns from extended objects such as buildings appear point-like. As a result, while in some images an object may be highly visible, in others it may be undetected. For example, one can look at two areas across images, marked in Fig. 7 (e) and corresponding to areas A and D in Fig. 4. For the tower at the upper right corner in the image, the change in echo intensity was measured to be up to nearly 30 dB across all images, and for the Medical School at the lower left part of the building this can be up to 20 dB (Table 2).

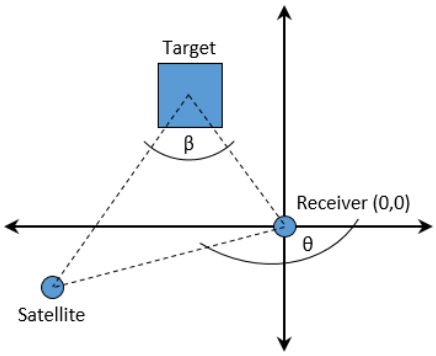

Figure 6: Bistatic imaging geometry

Table 2: Examples of intensity change across images

Target	Minimum Intensity (dB)	Maximum Intensity (dB)	Difference (dB)
A	-42.35	-13.71	28.64
D	-39.52	-19.78	19.74

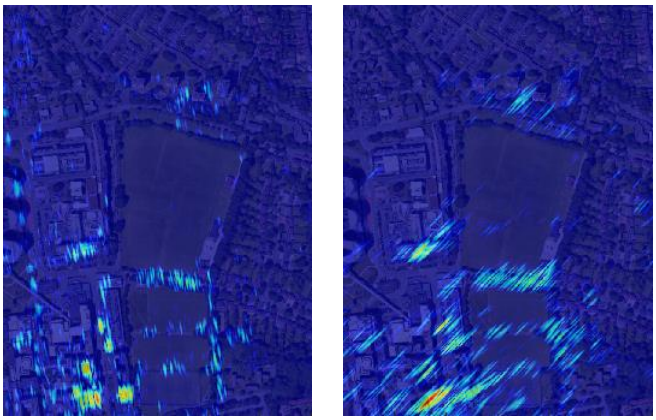

Left: (a) β=53.27˚, θ=76.30˚-70.71˚
Right: (b) β=61.78˚, θ=70.96˚-68.39˚

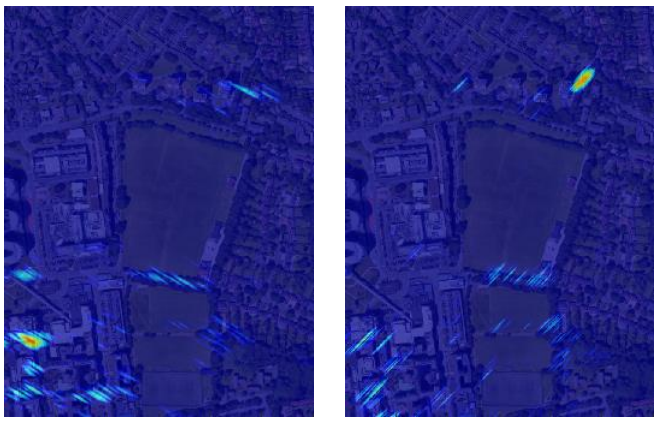

Left: (c) β=43.30˚, θ=88.75˚-91.16˚
Right: (d) β=87.99˚, θ=184.07˚-126.40˚

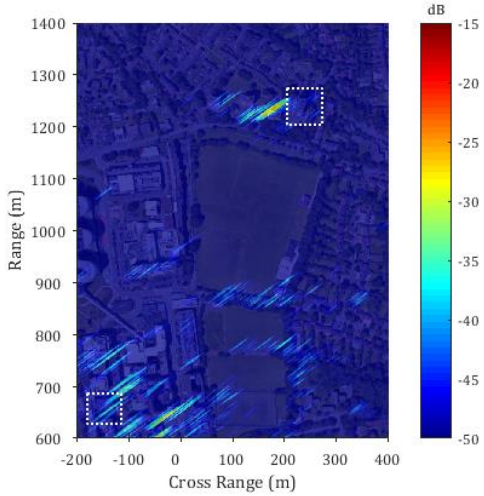

(e) β=79.98˚, θ=83.62˚-74.79˚

Figure 7: Example bistatic images obtained from (a) Galileo GSAT-0205-24 E5a, (b) GPS BIIF-05-30 L5, (c) Galileo GSAT-0214-05 E5a, and (d)-(e) GPS BIIF-07-09 L5

5. Multistatic Results and Analysis

To obtain a multistatic image, individual bistatic images were subsequently combined using Eq. 2. The image obtained using all 46 images is presented in Fig. 8 in a manner similar to those of the bistatic images.

Comparing the multistatic image to the bistatic images, it is visually clear that the multistatic image is a substantial improvement in terms of the information contain within. Several enhanced features of targets can be observed from the image, including edge and shape, which were not possible to observe with any single bistatic image due to the resolution and bistatic scattering effects.

From Fig. 8, outlines of the target B were visibly highlighted. These tree lines were in the middle of the scene (700 to 900 m range) and towards its far range (~1200 m range). The outline also includes a tree cluster at (~750 m range, 200 to 300 m cross range). The tree lines in the middle of the scene comprised horizontally and vertically oriented lines which enabled an upside down and inverted L-shape outline. The outline just below the residence towers is a row of trees following a road, which was not visible on its own before.

The targets A at the far end of the scene are identifiable. Among those towers, the rightmost tower had the

strongest reflection which is possibly due to its largest dimensions and metal structure on its roof, as well as the acquisition geometries (e.g. Fig. 7 (d)).

The target C, at ~0 cross-range just above the target B, oriented as a wall facing towards the receiver. The edge of its front and right sides were noticeable. The vertical edge of the target E (~700 to 850 m range, 0 to 50 m cross range) was also pronouced. In the following sub-sections, the potential to identify building shapes and estimate buildings dimensions is examined more closely.

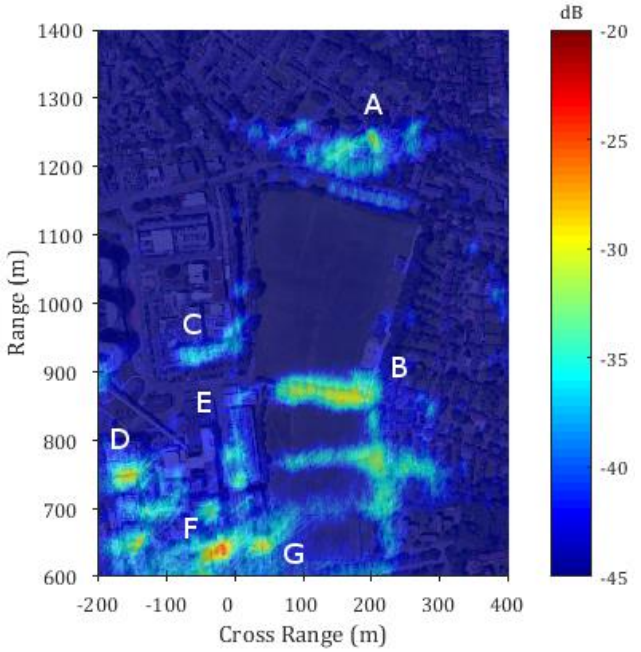

Figure 8: Multistatic SAR image, obtained by non-coherent addition of 46 bistatic SAR images

5.1. Identifying Building Shapes

The multistatic image reveals not only edges but also shapes of the targets. These geometric details can be seen across the image especially in the lower left of the image, which was previously difficult to gauge from individual bistatic images.

Reflections from the target D, at approximately 650 to 750 m range and -200 to -100 m cross range, were visible as a Pi-shape. Since the middle buildings had lower height than the surrounding, shadowing effects can be anticipated. Moreover, reflections from the middle part of the building were blocked at most bistatic geometries utilised.

The lower part of the target F (600 to 650 m range, -100 to 0 m cross range) and its adjacent buildings was oriented as an L-shape with one side of the wall behaves as a wall towards the receiver. It, therefore, behaved as a corner reflector. As a result, a high intensity reflection can be observed from this part. The reflection was seen as an L-shape as their actual shape. On the right of the target F was a part of target G with one side of the wall is facing towards the receiver. Hence a presence of this side can be detected with a strong return.

The ability to identify shapes in the image can be further demonstrated by applying standard edge detection techniques. In this case, a standard edge detection algorithm from MATLAB (a Robert detector) was applied to both bistatic and mutistatic images. Examples of edge detection results from bistatic images of Fig. 7 (b)-(e) are shown in Fig. 9 (a)-(d). Edge detection results from the multistatic image of Fig. 8 are shown in Fig. 9 (e), where scene structure is much more clearly pronounced than in any individual bistatic result.

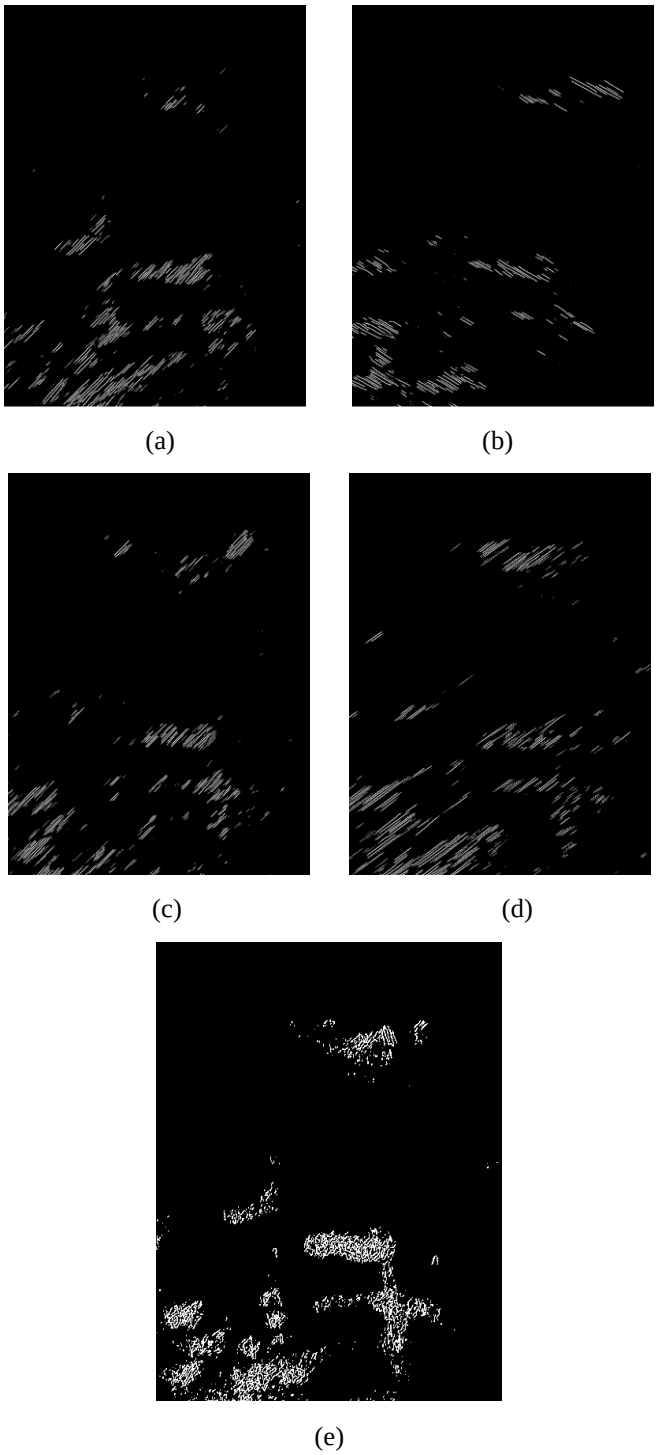

Figure 9: Edge detection results based on: (a)-(d) bistatic results shown in Fig. 7 (b)-(e), respectively, and (e) multistatic image in Fig. 8.

5.2. Examining Target Dimensions

It was previously shown that multistatic imagery can reveal edges and shapes. The next step is to identify whether it can provide estimates of object dimensions. Buildings in target area D (the IBR and the Medical School) were used for this purpose. Figure 10 shows enlargements of the individual bistatic images of Fig. 7, the multistatic image of Fig. 8, and

the corresponding Google Earth photograph. It can be seen that in the individual bistatic images it is not possible to estimate building dimensions, but this might be possible in the multistatic image. Building dimensions were estimated by measuring the extent of target responses in the image. Those were then compared to the dimensions of the building, measured from Google Earth satellite photographs. The obtained results for the two buildings in Fig. 10 (e) are shown in Tables 3 and 4.

Measured dimensions of both buildings from the multistatic image (Fig. 10 (e)) and the reference were comparable within 5 m.

Table 3: Dimensions of the IBR building

Image	Length	Width
Photograph	50.50 m	45.35 m
Multistatic Image	50.53 m	44.55 m
Difference	0.03 m	0.80 m
% Difference	0.05	1.76

Table 4: Dimensions of the Medical School building

Image	Length	Width
Photograph	34.32 m	22.43 m
Multistatic Image	30.41 m	25.23 m
Difference	3.91 m	2.80 m
% Difference	11.39	12.48

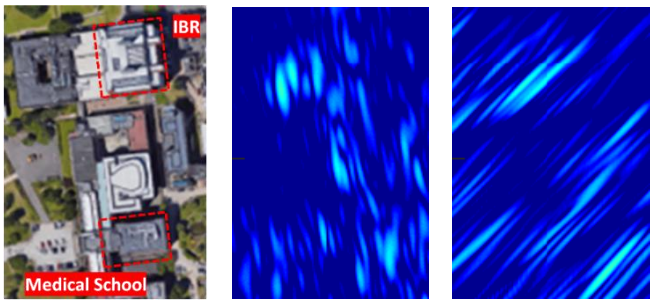

Left: (a) Google Earth photograph of target D
Middle:(b) Bistatic image (Fig. 7 (a))
Right: (c) Bistatic image (Fig. 7 (b))

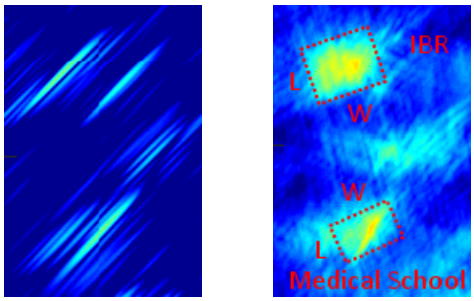

(d) Bistatic image (Fig. 7 (d)) (e) Multistatic image

Figure 10: Dimensions measurement for the target D

5.3. Multi-bistatic Scattering Properties

In this section, instead of combining the 46 bistatic images onto a single image, information contained within the images was combined. In particular, variations on the returned echo strength of two different types of objects, trees and man-made structures, were recorded and plotted on the same graph. The idea to be tested is that since different types of objects scatter differently at different bistatic angles, it may be possible to use this effect to provide a rough object classification. As oppose to more complex algorithm, objects can be distinguished by observing variation in their echo strengths over a range of bistatic angles.

The objects under test where the four towers in target area A (shown in Fig. 11 (a)), where tower 4 is the largest and towers 1-3 are very similar, if not the same, in terms of dimensions, and trees in target area B (Fig. 11 (b)).

The intenstity of each of the towers in area A was recorded for all 46 images and is plotted in Fig. 12 (a). Similarly, the intensity of the 8 trees in area B is plotted in Fig. 12 (b). The vertical axes in both figures are the same as those used so far, i.e. 0 dB represents the highest intensity of the compressed direct signal across all bistatic images, and -50 dB is the lower end of the dynamic ranges in the images shown so far. Note that the plots in Fig. 12 (a) are not continuous. This is because at certain images, the bistatic geometries were such that the intensity of the returns from towers was below the dynamic range set. Finally, results are shown with image no. as the horizontal axis, as opposed to bistatic angle or satellite azimuth angle, where image no. 1-12 corresponds to GPS BIFF-05-30 L5, image no. 13-24 and image no. 25-36 correspond to Galileo GSAT-0205-24 E5a and E5b respectively, image no. 37-41 corresponds to Galileo GSAT-0214-05 E5a, and image no. 42-46 corresponds to GPS BIIF-07-09 L5, with relative geometries as indicated in Table 1. This was because different images have very similar bistatic angles, but different azimuth angles, or vice versa. Therefore, to plot echo intensity as a function of either becomes problematic, and so does its interpretation. As a first step here, the objective is to identify whether there is substantial variation in echo intensity as a function of acquisition geometry, to justify a further, more detailed investigation.

Starting from Fig. 12 (b), it can be seen that all trees in the area have a similar variation in terms of intensity across all images and within a span of approximately 5 dB, which means that it is practically independent of the bistatic acquisition geometry. This could be expected since at L-band the major contribution from tree reflections comes from their trunks, and those could be approximated as cylindrical in shape.

Conversely, Fig. 12 (a) shows a much larger variation in signal strength for the four towers, and especially tower 4 which is physically the largest. In particular, there are returns which are below the dynamic range, while at other angles they can be up to 25 dB below the direct signal. For returns within the dynamic range, intensity variations span approximately 25 dB. More interestingly, maximum intensities are obtained at specific acquisition geometries. This could also be expected, since the main contributors to echo strength in this case are building walls. Therefore, if the relative geometry between the transmitter, the building wall, and the receiver enables specular reflections to be recorded by the receiver, the expected echo strength would be substantially increased. To investigate this further, note that tower four is almost in the direct line-of-sight of the receiver (Fig. 11 (a)).

At the tower four, maximum returns can be observed from image no. 16, 28, and 43. For image no. 16 and 28, the tower four was observed by Galileo GSAT-0205-24 satellite with two different frequencies at 91.66 degrees in azimuth and 52.20 degrees in elevation, with a bistatic angle of nearly 53 degrees. This satellite position was exactly behind the

receiver and hence enabled specular reflections as anticipated. What is not as clear is the high echo strength for image no. 43 (GPS BIFF-07-09), where the satellite was at an azimuth of 155.24 degrees and elevation of 85.20 degrees and the bistatic angle was 88 degrees. In this case, the strong return from the tower cannot be explained purely from a geometrical perspective, indicating some more complex scattering mechanisms. Therefore, further study to comprehend the relationship between imaging geometry and scattering properties will be included in the future work.

The obtained results show that using multiple bistatic images, a first classification of object types within a scene could be obtained.

(a)

(b)

Figure 11: Enlargements of Fig. 4 around (a) area A, (b) area B

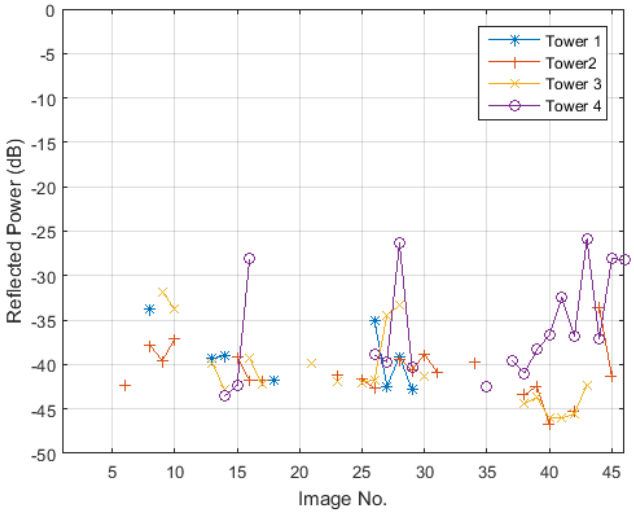

(a)

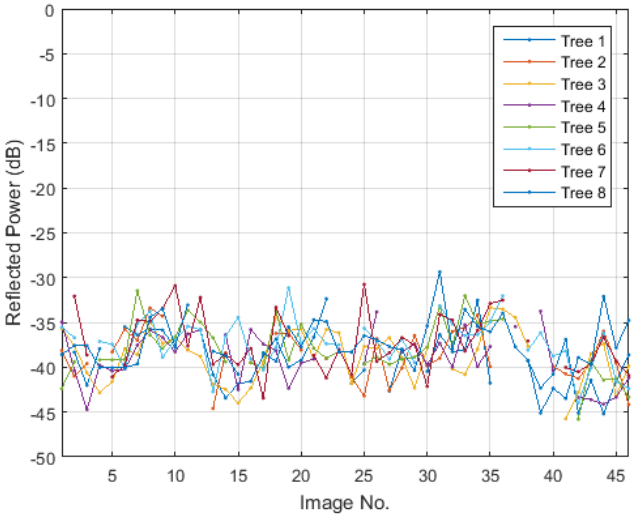

(b)

Figure 12: Variations in echo strength across 46 bistatic images for (a) towers in area A, (b) trees in area B

6. Conclusions and Future Work

This paper explored the potential of a passive multistatic SAR using navigation satellite as transmitters of opportunity. A measurement campaign was conducted for acquiring signals from multiple satellites simultaneously, using an experimental testbed over the duration of few hours. A total of 46 bistatic images were obtained based on the total recording time. A multistatic SAR image was first formed by non-coherent addition of those bistatic images. This multistatic image showed a drastic improvement over the bistatic SAR image despite utilising a basic combination technique, despite the spatial resolution of individual images is limited. It can not only detect the presence of targets but also reveal geometric features, such as edge, shape, and dimensions. In addition, it was shown that by exploiting object scattering variations across a series of bistatic imaging geometries, a first order classification of objects within the scene is possible. Future work will investigate more advanced combination techniques, and tools for feature extraction and object type classification based on obtained multistatic results.

7. References

[1] D. Gromek, K. Kulpa, and P. Samczyński, "Experimental Results of Passive SAR Imaging Using DVB-T Illuminators of Opportunity," *IEEE Geosci. Remote Sens. Lett.*, vol. 13, no. 8, pp. 1124–1128, Aug. 2016.

[2] L. M. H. Ulander, P. O. Frölind, A. Gustavsson, R. Ragnarsson, and G. Stenström, "Airborne passive SAR imaging based on DVB-T signals," in *2017 IEEE IGARSS*, Fort Worth, TX, 2017, pp. 2408–2411.

[3] P. Marques, A. Ferreira, F. Fortes, P. Sampaio, H. Rebelo, and L. Reis, "A pedagogical passive RADAR using DVB-S signals," in *2011 3rd Int. APSAR*, Seoul, 2011, pp. 1–4.

[4] M. Antoniou and M. Cherniakov, "GNSS-based bistatic SAR: a signal processing view," *EURASIP J. Adv. Signal Process.*, vol. 2013, no. 1, pp. 1–16, Dec. 2013.

[5] M. Antoniou, Z. Zeng, F. Liu, and M. Cherniakov,

"Experimental demonstration of passive BSAR imaging using navigation satellites and a fixed receiver," *IEEE Geosci. Remote Sens. Lett*., vol. 9, no. 3, pp. 477–481, May 2012.

[6] H. Ma, M. Antoniou, and M. Cherniakov, "Passive GNSS-based SAR resolution improvement using joint Galileo E5 signals," *IEEE Geosci. Remote Sens. Lett*., vol. 12, no. 8, pp. 1640–1644, Aug. 2015.

[7] H. Ma *et al*., "Galileo-based bistatic SAR imaging using joint E5 signals: experimental proof-of-concept," in *Int. Conf. Radar Systems*, Belfast, 2017, pp. 1-5.

[8] F. Santi, M. Bucciarelli, D. Pastina, M. Antoniou, M. Cherniakov, "Spatial resolution improvement in GNSS-based SAR using multistatic acquisitions and feature extraction," *Trans. Geosci. Remote Sens*., vol 54, no. 10, pp. 6217-6231, Oct. 2016.

[9] T. Zeng *et al*., "Multiangle BSAR imaging based on BeiDou-2 navigation satellite system: experiments and preliminary results," *IEEE Trans. Geosci. Remote Sens*., vol 53, no. 10, pp. 5760-5773, Oct. 2015.

[10] M. Antoniou and M. Cherniakov, "GNSS-based passive radar," in *Novel Radar Techniques and Applications Volume 1: Real Aperture Array Radar, Imaging Radar, and Passive and Multistatic Radar*, R. Klemm, U. Nickel, C. Gierull, P. Lombardo, H. Griffiths and W. Koch, Eds. London, UK: IET, 2017, ch. 16, pp. 719-766.

[11] R. Zuo, "Bistatic synthetic aperture radar using GNSS as transmitters of opportunity," Ph.D. dissertation, School Electron. Elect. Comput. Eng., Univ. Birmingham, Birmingham, UK, 2011.

[12] M. Cherniakov and T. Zeng, "Space-surface bistatic SAR," in *Bistatic Radar: Emerging Technology*, M. Cherniakov, Ed. Chichester, UK: John Wiley & Sons, 2008, ch. 6, pp. 215-246.